



## Experimental and Numerical Investigation of the Influence of Leading Edge Tubercles on S823 Airfoil Behavior

R. Supreeth<sup>1†</sup>, A. Arokkiaswamy<sup>2</sup>, K. Anirudh<sup>3</sup>, R. K. Pradyumna<sup>3</sup>, P. K. Pramod<sup>3</sup> and A. K. Sanarahamat<sup>3</sup>

<sup>1</sup>*Department of Aeronautical Engineering, Dayananda Sagar College of Engineering, Department of Aerospace Engineering, Rashtriya Vidyalaya College of Engineering, Bengaluru, Karnataka, 560059 India*

<sup>2</sup>*Department of Aeronautical Engineering, Dayananda Sagar College of Engineering, Bengaluru, Karnataka, 560078, India*

<sup>3</sup>*Department of Aerospace Engineering, Rashtriya Vidyalaya College of Engineering, Bengaluru, Karnataka, India*

† *Corresponding author e-mail: [supreeth@rvce.edu.in](mailto:supreeth@rvce.edu.in)*

(Received December 13, 2019; accepted May 25, 2020)

### ABSTRACT

Investigating the role of leading edge tubercles on the aerodynamic behavior of S823 airfoil tailored for wind turbine applications has been the forefront of the study. The aerodynamic characteristics of S823 airfoil effectuated by leading edge tubercles are ascertained at Reynolds number  $Re=200000$  which is the usual operating range of most of the small-scale wind turbines. Firstly, the study elucidates the numerical investigation of baseline airfoil and later modified airfoils exhibiting different amplitude  $A$  and wavelength  $\lambda$  of the sinusoidal leading edge tubercles represented as A07W50, A12W50, and A07W25. The aerodynamic characteristics of the airfoils at  $Re=200000$  and angles-of-attack ranging from  $0^\circ$  to  $20^\circ$  are evaluated numerically through  $k-\omega$  SST turbulence model using ANSYS FLUENT<sup>®</sup> software package. A preliminary comparison of the computational data shows that the coefficient of lift  $C_l$  of all the modified airfoils was visibly superior to the baseline model across the angles tested. A07W50, A12W50 and A07W25 registered 20.6%, 26.2%, and 8.7% increase in the  $C_l$  values as compared to the baseline model. Contrasting to the  $C_l$  values, the aerodynamic efficiency  $C_l/C_d$  of the baseline model was slightly better but only across the pre-stall regime and later culminated with a sudden hard stall. Promisingly, this type of hard stall was not true for the tubercled models that demonstrated a more gradual and restrained stalling characteristic, thus showcasing superior performance in the post stall envelope that was never observed for the baseline model. Based on the outcomes, A07W50 model that displayed better aerodynamic characteristics was eventually fabricated and experimentally tested for its performance in a low speed wind tunnel. The numerical results of A07W50 were in good agreement with the experimental results. The overall results of the study prove beyond any point of doubt that tubercles indeed aid in improving the aerodynamic characteristics by enhancing the lift Coefficient  $C_l$ , rendering soft stalling nature and extending the scope of operation for the airfoil under study. Finally, the study positively confirms that leading edge tubercles very much play a significant role in passively augmenting the fluid dynamic characteristics of S823 airfoil and also qualify them to be a competitive passive flow control device.

**Keywords:** Aerodynamic characteristics; Humpback whales; Passive flow control; Flow separation; Leading edge tubercles.

### NOMENCLATURE

$A$	amplitude of tubercle	$C_l/C_d$	coefficient of lift to coefficient of drag
$AR$	Aspect Ratio of the Airfoil	$Re$	Reynolds Number
$\alpha$	angle-of-attack	$U_0$	free stream velocity
$c$	chord length of the airfoil		
$C_l$	coefficient of lift of the airfoil	$\lambda$	wavelength of tubercle
$C_d$	coefficient of drag of the airfoil		

## 1. INTRODUCTION

Flow separation is a fundamental problem affecting the performance of every other fluid dynamic system in existence. Flow separation can commonly be witnessed on airfoils and wings at large angles of attack  $\alpha$ . Effects of separated flow are no less important in compressors, pumps, propellers, helicopters, missiles, diffusers, nozzles, UAVs, wind turbines, marine vehicles (Gad-el-Hak and Bushnell 1991; Gad-el-Hak 1989 and Zanin *et al.* 2012) and many more. Since most of the fluid systems are invariably influenced by flow separation, managing it is of prime importance. Controlling flow separation by either passively or actively manipulating the flow postpones its occurrence and apparently augments the fluid dynamic performance (Gad-el-Hak 1998). For obvious reasons great efforts have been made towards the development of numerous flow control techniques. In monograph, they are termed as active and passive flow control techniques. Active flow controls (AFCs) seamlessly rely on feedback schemes constantly monitoring the flow field on real time basis and regulate the flow complying with optimum flow conditions (Jahanmiri 2010). Though AFCs demonstrate large potential payoffs, the involvement of complex electronics architecture makes the process laborious, complicated and also an expensive process to reckon with (Jahanmiri 2010). But, on the flipside, attributing to their simplicity Passive flow control (PFC) technique is gaining much importance contrasted to their competitors (Moghaddam *et al.* 2017). PFCs aid in passively transiting the fluid from laminar to turbulent regime by energizing the boundary layer. Vortex generators, leading/trailing edge modifications and, Gurney flaps are few examples for PFCs (Akshoy Ranjan *et al.* 2013). Nevertheless, the work of Fish and Battle in the field of Biomimicry has showcased the tubercles of the humpback whales as an excellent candidate for passive flow control devices (Fish *et al.* 2013). Humpback whales are large marine animals, best known for their gigantic physical appearance as well as agile acrobatic nature. From field observations by marine biologists, it is suggested that the tubercles of the humpback whale act as a passive flow control devices (Choi *et al.* 2012; Fish *et al.* 2011; Fish *et al.* 2006 and Fish *et al.* 2008). In hydrodynamic perspective, tubercles cause the flow to remain attached to the flipper over large angles of attack, thus holding up the flow from separating. Delaying flow separation eventually leads to greater lift (Bharat Bhushan 2009 and Bar-Cohen 2006), enabling the whale to execute tight turns, roll, leap, break, breach, hunt at ease. This encompassing feature of the humpback whales exhibits an improved hydrodynamic behavior (Fish 2006 and Fish *et al.* 2013). In many engineering practices, the flow phenomenon occurring over the humpback whale flippers closely mimics the flow over airfoils and hydrofoils. Understanding leading edge tubercles in detail may offer potential benefits in the field of fluid dynamics that may help in passively amplifying the flow behavior of airfoils and hydrofoils.

A morphological survey carried out by Fish *et al.*

(1995) suggest that the humpback whale flipper closely simulates a NACA 634-021 airfoil and passively controls the fluid flow. Watts *et al.* (2001) documented that the wings with protuberances offered an additional 4.8% and 17.6% of lift and lift-to-drag ratio against wings without leading edge tubercles. Through wind tunnel tests Miklosovic *et al.* (2014) hypothesized the tubercles to be analogous to vortex generators that increase momentum exchange across the boundary layer. Detailed experiments conducted by Johari *et al.* (2007) showed the shorter wavelength and longer amplitude of the protuberance to be the dominant factors affecting the flow characteristics of an airfoil particularly beyond the stall regime. The isosurface plots for a scalloped flipper model obtained by Hugo *et al.* (2008) employing numerical Detached Eddy Simulation (DES) turbulence scheme demonstrated that the vortices re-energize the boundary layer by accelerating a momentum transfer across the shear layers and delays flow separation. Experiments conducted by Hansen *et al.* (2009) on various tubercle morphology, inferred that low amplitude and low wavelength combinations are more effective in controlling the early boundary layer separation experienced in laminar flows where the momentum exchange is poor. From the experimental outcomes Miklosovic *et al.* (2007) postulated that scallops render a three-dimensional vortex flow over the wing and thereafter curtails the spanwise stall progression leading to a larger operating regime. Flow visualization studies conducted by Weber *et al.* (2011) highlighted the existence of the attached flow along the span of the tubercled model even at steep angles of attack. Rostamzadeh *et al.* (2013) indicated that the tubercled model induces periodically varying circulation very similar to vortex generation along with the streamwise movement of the flow. The computational outcomes performed by Lohry *et al.* (2012) showed that the effects of tubercles are found to be ineffective only at lower Reynolds numbers. At higher Reynolds number flows, tubercles act as vortex generator that successfully helps in boundary layer energization and mitigate stall effects at higher attack angles. With the aid of Particle Image Velocimetry technique Shi *et al.* (2017) proved that the tubercles are solely responsible for generating additional torque on the wind turbine blades due to the attached flow at deep stall angles.

The outset of the extensive literature review showcases the leading edge tubercles to enhance the aerodynamic characteristics of airfoils and wings. Despite significant experimental and numerical contributions from various researchers, there is still enough scope to ascertain the role of tubercles in enhancing the fluid dynamic behavior of airfoils. Further, most of the researches on tubercles have been aimed at general application airfoils and there is a dearth of information on ascertaining the effect of tubercles on airfoils developed for the wind turbines. Hence, efforts are made in the current study to understand how tubercles would benefit in aiding better flow characteristics to an airfoil specifically developed for horizontal axis small

scale wind turbine blades.

In the underlying bio-mimetic research work, the effect of sinusoidal leading edge tubercles on the aerodynamic behavior of NREL S823 airfoil for the horizontal axis small scale wind turbine blades are first numerically investigated using ANSYS FLUENT® software package. The aerodynamic characteristics of the baseline and three modified airfoils with different amplitude  $A$  and wavelength  $\lambda$  are tested using  $k-\omega$  SST turbulence model at Reynolds number  $Re=200000$  across varying degrees of angles-of-attack  $\alpha$ . The coefficient of lift ( $C_l$ ), drag ( $C_d$ ) and the aerodynamic efficiency ( $C_l/C_d$ ) of the airfoils are ascertained slightly beyond stall angles. Computational outcomes of the modified airfoils will be compared with the baseline airfoil for the parameters considered. Finally, the modified airfoil exhibiting comparably the best aerodynamic behavior will be fabricated and experimentally tested in a low speed wind tunnel to validate the role of leading edge tubercles.

## 2. NUMERICAL SIMULATION METHODOLOGY

### 2.1 Geometry Details

In this investigation, S823 airfoil jointly developed by National Renewable Energy Laboratory (NREL) and Airfoils Inc., categorically for stall regulated small scale horizontal axis wind turbines is considered. S823 airfoil is a highly specialized airfoil designed for wind turbines of capacities from 2kW to 10kW (Tangler *et al.* 1995). The NREL S series airfoils are known for Low Reynolds number performance in combination with insensitivity towards leading edge roughness (Lyon *et al.* 1995) that renders great aerodynamic benefits compared to traditional airfoils. NREL S823 airfoil exhibits an unsymmetrical profile with maximum thickness and camber of 21.2% and 2.4% occurring at 24.3% and 70.5% of the chord  $c$  respectively. The geometrical profile of the S823 airfoil is illustrated in Fig. 1.

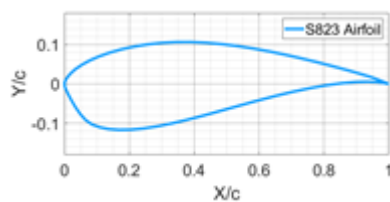


**Fig. 1. Illustration of S823 airfoil cross sectional profile.**

Additionally, to evaluate the role of tubercles, the leading edge of the baseline model is remodified for three differing cases each furnished with unique amplitude  $A$  and wavelength  $\lambda$ . Modified models are designated as A07W50, A12W50, and A07W25, where the suffixed numbers represent the amplitude  $A$  and wavelength  $\lambda$  of the tubercle as a percentage of chord  $c$ . The selected amplitude and wavelength are found to be efficient in controlling the fluid dynamic characteristics of airfoils as reported in Johari *et al.*

(2007), Guerreiro *et al.* (2012), and the same has been adopted in the current study. The geometrical details of the baseline and the modified models are provided in tables 1 and 2 and their geometrical rendering in CATIA V5R19 software package is illustrated in Fig. 2.

**Table 1 Geometric Characteristics of Baseline S823 Airfoil**

Chord (c) mm	Span (b) mm	Aspect ratio (b/c)	Thickness (%)	Max camber (%)	X/c max thickness (%)	X/C max camber (%)
Baseline Airfoil						
150	600	4	21.2	2.4	24.3	70.5
A07W50 Modified Airfoil						
150	600	4	21.2	2.4	24.3	70.5
A12W50 Modified Airfoil						
150	600	4	21.2	2.4	24.3	70.5
A07W25 Modified Airfoil						
150	600	4	21.2	2.4	24.3	70.5

**Table 2 Details of Modified S823 airfoil**

Airfoil	Amplitude (A)	Wave length ( $\lambda$ )	A/ $\lambda$ ratio
A07W50	0.07 c	0.50 c	0.14
A12W50	0.12 c	0.50 c	0.24
A07W25	0.07 c	0.25 c	0.28

### 2.2 Numerical Simulation

In this section, the aerodynamic behaviour of baseline and the modified airfoils has been extensively studied using ANSYS FLUENT® software. Leading edge tubercles induce localized 3D spanwise movement in the flow and to comprehend the problem, 3D steady incompressible viscous flow condition has been assumed in the analysis with second order pressure interpolation scheme. Second order pressure interpolation scheme performs extremely well for continuous, pressure gradient flows. Since the performance of the interpolation scheme is also influenced by the initial guess, the first few iterations were run for pseudo – transient conditions with a pseudo – time step of 0.0001 seconds. The solver was then switched over to transient conditions for further iterations. The equations characterizing the steady incompressible viscous flows are the Continuity and Reynolds averaged Navier–Stokes (RANS) equations as expressed by Eq. (1) & Eq. (2).

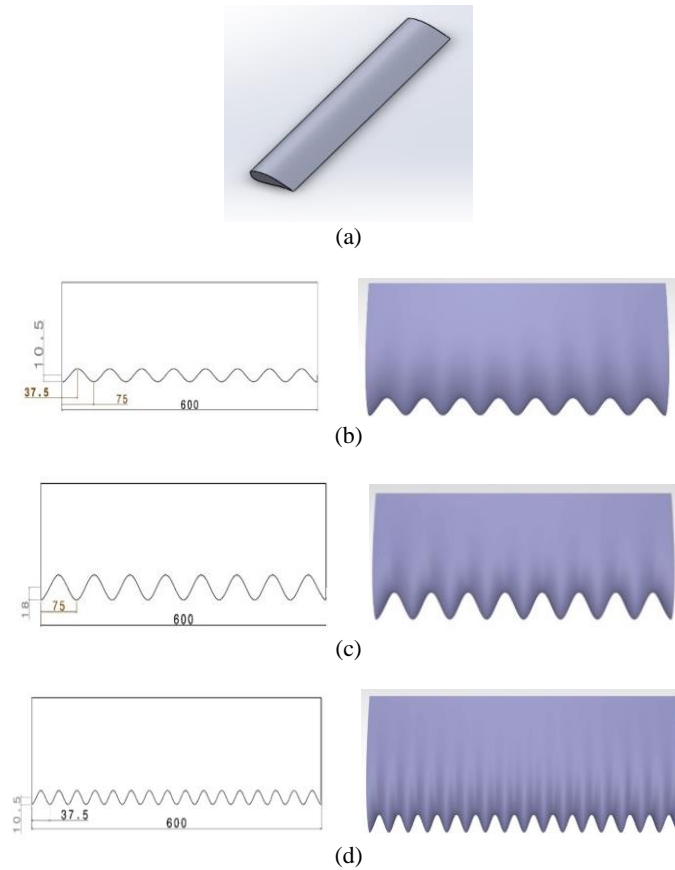


**Fig. 2. (a) Isometric View of Baseline Airfoil, (b) Top View of A07W50, (c) A12W50 and (d) A07W25 modified models-All Dimensions in mm.**

$$\frac{\partial \bar{U}_i}{\partial x_i} = 0 \quad (1)$$

$$\rho \bar{u}_j \frac{\partial \bar{u}_i}{\partial x_j} = -\frac{\partial \bar{p}}{\partial x_i} + \mu \frac{\partial}{\partial x_j} \left[ \frac{\partial \bar{u}_i}{\partial x_j} + \frac{\partial \bar{u}_j}{\partial x_i} \right] - \frac{\partial}{\partial x_j} (\rho \bar{u}_i \bar{u}_j') \quad (2)$$

where the total convective change in mean momentum is represented by the term on the left hand side of the equation, which is balanced by mean pressure field, stresses developed due to the viscous term and the Reynolds stress generated by the velocity fluctuations (represented by the last term of Eq.(2)). Here,  $\rho$  is the density ( $\text{kg/m}^3$ ),  $\mu$  is the fluid viscosity ( $\text{N}\cdot\text{s/m}^2$ ),  $\bar{u}_i'$  and  $\bar{u}_j'$  are the velocity fluctuation components (m/s), the subscripts  $i$  and  $j$  are the free indices with  $i$  and  $j = 1, 2, 3$  representing  $x, y$  and  $z$  directions respectively and  $\bar{p}$  is the mean pressure (Pa). The additional modeling to obtain Reynolds stress term is satiated with the use of  $k-\omega$  SST model. Despite the availability of differing advanced turbulence models,  $k-\omega$  SST turbulence model has been employed. The use of a  $k-\omega$  SST formulation in the sub layers of the boundary layer makes the model more usable at the near-wall and far-field zones. Further, the  $k-\omega$  SST model has good capabilities to accurately determine the flow properties for a wide range of flows as compared to the standard  $k-\epsilon$

turbulence model. Also,  $k-\omega$  SST model can be invoked in the absence of any extra damping functions to solve the Low Reynolds turbulence model. The equations are solved by the Pressure-Velocity Coupling algorithm with a second order spatial discretization scheme based on the Finite Volume Method (FVM). The convergence criterion of  $1 \times 10^{-5}$  and 30 iterations per step are used in the analysis and the relevant data can be inferred from table 3.

**Table 3 Numerical Simulation Details**

Solution Controls		Boundary Condition	
Turbulent Kinetic Energy	1	Inlet	Velocity Inlet of 20 m/s in x-axis
Specific Dissipation Rate	0.95	Outlet	Pressure Outlet with 0-gauge pressure
Solution		Method	
Residuals	$1 \times 10^{-5}$	Pressure-Velocity Coupling	Coupled
Time Step Size	0.0001	Spatial Discretization	Second order upwind
Time Steps	50,000	Transient Formulation	Second Order Implicit

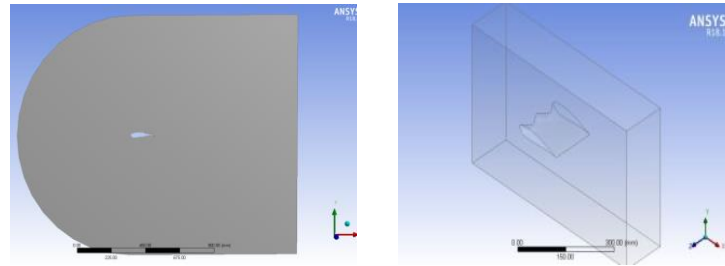


**Fig. 3. Display of the domains for the baseline and modified models.**

**Table 4 Grid details of baseline S823 airfoil**

Mesh	1	2	3	4	5
Elements	56326	70482	80552	92019	98196
Orthogonality	0.78	0.58	0.61	0.52	0.43
Max Aspect Ratio (AR)	4.6	7.0	6.9	1.0	1.2
Wall Y+	5.845	3.428	2.01	0.98	0.910
C <sub>l</sub> at 0°	0.192	0.221	0.251	0.280	0.295

Figure 3 displays the coordinate system, boundary conditions, and the computational domains of the baseline and the modified models. A fixed Cartesian coordinate system (x, y) is used. The origin of the domain is located at the start of the airfoil leading edge. The x-axis is aligned with the inlet flow direction. The size of the C-shaped domain is defined by a radius of 8c and a far-field radius of 10c, whereby c represents the mean chord length of the airfoil, which is 150 mm and cuboid shaped domain for modified airfoil is defined by the length of 10c and the height of 4.5c with symmetric boundary condition on far-field for a total span of 600mm. No-slip boundary and symmetry conditions were applied unanimously for all the airfoils. The uniform flow with low turbulent intensity and the free stream velocity (U<sub>0</sub>) is imposed on the inflow boundary condition along x-axis. The pressure outlet condition at 0-gauge pressure is applied to the outflow boundary. The computations for the flow around the S823 airfoil section is performed at the Reynolds number Re=200000 for angles-of-attack of 0° to 20° with a step length of 1°. S823 airfoil being specifically designed for horizontal axis wind turbines, we try to analyze the airfoil behavior at a free stream velocity of U<sub>0</sub>=20m/s. Based on the wind tunnel test section dimensions, the chord length of the airfoil is fixed at c=0.15m. For the wind velocity and the chord length scale, the corresponding Reynolds number which is defined as the ratio of inertial forces to viscous forces is calculated from Eq. (3).

$$Re = \frac{\rho U_0 l}{\mu} = \frac{U_0 l}{\nu} = \frac{20 \cdot 0.15}{1.50 \cdot 10^{-5}} = 200000 \quad (3)$$

Where, ρ (kg/m<sup>3</sup>) is the density of the fluid, U<sub>0</sub> (m/s) is the flow speed, c (m) is the characteristic chord length of the airfoil, μ (N·s/m<sup>2</sup>) is the dynamic viscosity of the fluid, ν (m<sup>2</sup>/s) is the kinematic viscosity of the fluid. Eventually, the lift and drag forces were obtained directly from

ANSYS Fluent and the corresponding C<sub>l</sub> & C<sub>d</sub> were ascertained from Eq. (4) & Eq. (5).

$$C_l = \frac{2l}{\rho U_0^2 S} \quad (4)$$

$$C_d = \frac{2d}{\rho U_0^2 S} \quad (5)$$

where C<sub>l</sub> is the coefficient of lift, l (N) is the lift force, C<sub>d</sub> is the coefficient of drag, d (N) is the drag force, ρ is the fluid density (kg/m<sup>3</sup>), U<sub>0</sub> (m/s) is the free stream velocity of the fluid, S (m<sup>2</sup>) is the surface area of the airfoil.

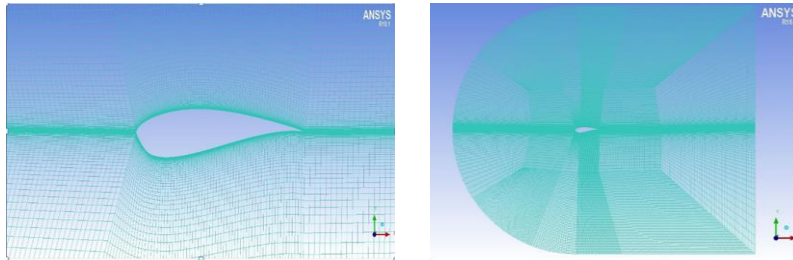
### 2.3 Mesh Details

Table 4 and Fig. 4 indicate the grid distribution details for the baseline model. A fine structured quadrilateral mesh in 2-D is achieved in the vicinity of the airfoil that gradually coarsens towards the surface. The averaged minimum grid spacing on the airfoil surface of 3.41 × 10<sup>-5</sup> m corresponds to y+ of 0.91 as the wall unit. Similarly, the mesh and grid independence for the modified model is highlighted in Fig. 5 and table 5.

## 3. EXPERIMENTAL METHODOLOGY

### 3.1 Wind tunnel Details

Experimental investigations addressed in the succeeding sections were carried out in a low speed open circuit wind tunnel housed at the Department of Aerospace Engineering, R V College of Engineering, and the same is depicted in Fig. 6. The facility is a suction type tunnel consisting of a honeycomb inlet, followed by multi-level anti-turbulence screens, bell mouth with 9:1 contraction ratio, test section, diffuser, and the motor section at the rear end from the inlet section. The test section of the tunnel measured at 0.6m x 0.6m x 2m was



**Fig. 4. Grid distribution around S823 baseline airfoil.**

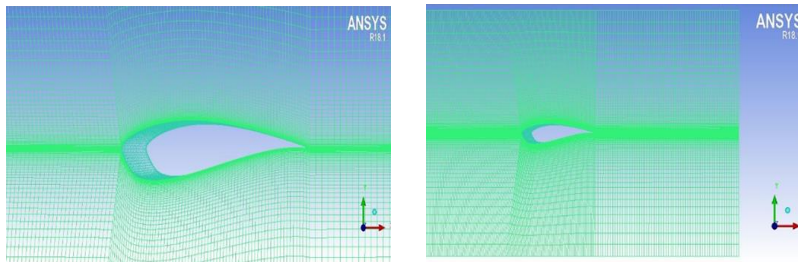


**Fig. 5. Grid distribution around modified S823 airfoil.**

**Table 5 Grid independent study of modified S823 airfoil**

Mesh	1	2	3	4	5
Elements (e6)	0.14	1.8	2.2	2.3	2.4
Orthogonality	0.49	0.43	0.48	0.36	0.38
Max AR	61	64	69	73	86
Wall Y+	6.05	3.986	2.021	1.323	0.973
$C_i$ at $0^\circ$	0.187	0.216	0.244	0.273	0.288



**Fig. 6. Low Speed Open Circuit Wind Tunnel.**

capable of achieving free stream velocities close to around 85m/s. The tempered acrylic glass windows of the test section offered excellent optical visualization. In conjunction with the honeycombs, the flow straighteners alongside the mesh functioned as conditioners to remove any non-axial components of the flow, thus ensuring minimal turbulence intensity of less than 2%.

### 3.2 Model Details

Based on the numerical outcomes, the modified model A07W50 with comparatively better

aerodynamic characteristics was fabricated. For the given amplitude and wavelength, eight tubercles of 18mm amplitude and 75mm wavelength were uniformly blended to the leading edge of the baseline model. The models were manufactured using fiber reinforced plastic (FRP) and the surface finish was maintained at 20  $\mu\text{m}$ . With the geometrical length of  $L=600\text{mm}$ , the models spanned the entire length of the tunnel test section. Finally, the models were given a dull black finish to reduce the illumination from the test section light source. The physical models of the baseline and

modified airfoils are displayed in Fig. 7.



**Fig. 7. Baseline and A07W50 Modified Airfoils.**

Experimental estimation of the aerodynamic properties of the baseline and the modified airfoils were accomplished through the pressure port technique. To facilitate the measurements, a pitot-static probe was installed at the exit plane of the tunnel nozzle. Further, the baseline airfoil was instrumented with 44 ports and the modified airfoil was equipped with 48 ports respectively. For Reynolds number  $Re=200000$ , the velocity of the free stream air in the test section was set at 20m/s. Calibration studies were duly performed on the tunnel and finally the local pressure variations across the airfoils were meticulously recorded for all angles of attack  $\alpha$ . From the pressure probes recordings, coefficient of Pressure  $C_p$  was calculated using the Eq. (6).

$$C_p = \frac{p - p_\infty}{q_\infty} \quad (6)$$

Where  $C_p$  is the coefficient of pressure,  $p$  is the static pressure (Pa),  $p_\infty$  is the free stream pressure (Pa) and  $q_\infty$  is the free stream dynamic pressure (Pa), represented as  $q_\infty = \frac{1}{2} \rho U_0^2$ . The coefficient

of pressure  $C_p$  for the respective angles of attack was plotted against  $X/c$  of the airfoil in MATLAB. Later the coefficient of normal force ( $C_n$ ) for each angle of attack  $\alpha$  was calculated in MATLAB through Eq. (7) & Eq. (8).

$$F_n = \int \Delta p ds \quad (7)$$

$$C_n = \frac{F_n}{q_\infty} \quad (8)$$

Where  $F_n$  is the normal force (N),  $\Delta p$  is the differential pressure measured in the static pressure port (Pa),  $ds$  is the surface of the airfoil over which the differential pressure is measured ( $m^2$ ),  $C_n$  is the coefficient of normal force and  $q_\infty$  is the dynamic pressure (Pa). Finally, the coefficient of lift  $C_l$  and coefficient of drag  $C_d$  were calculated using Eqs. (9) and (10) albeit without accounting for the viscous force.

$$C_l = C_n \cos \alpha \quad (9)$$

$$C_d = C_n \sin \alpha \quad (10)$$

The probable uncertainties propagated during the experimental investigation have been accounted for by adopting Kline McClintock uncertainty analysis presented by Kline and McClintock [35]. Thorough calibration studies performed for the wind tunnel proved to be almost free of any errors measured for a sample velocity of 10m/s. Velocity measurements carried out at multiple locations in the test section resulted in a meager uncertainty of less than 0.1%. Next, the adjustments in the angle of attack were done manually by aligning the pointer of the airfoil model with the graduations on an  $180^\circ$  angular protractor having the least count of  $1^\circ$  and facilitated with a magnifier. Assuming the largest error of  $0.25^\circ$  misalignments at a  $10^\circ$  sample test fetched a maximum uncertainty of 2.5%. Lastly, the uncertainties observed in the pressure port technique stood at 1.1%. Altogether, the total uncertainty of the experimental analysis was recorded to be well within 4%.

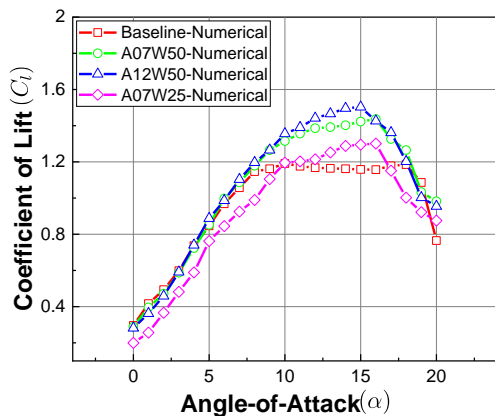
#### 4. RESULTS AND DISCUSSIONS

The ensuing section discusses the aerodynamic results of NREL S823 baseline and modified airfoils obtained both numerically and experimentally. The outcomes of the numerical simulation unravelled a significant amount of data that demystifies the capability of the leading edge tubercles on the performance of airfoils. The section first discusses the numerical aerodynamic results before proceeding towards the experimental outcomes.

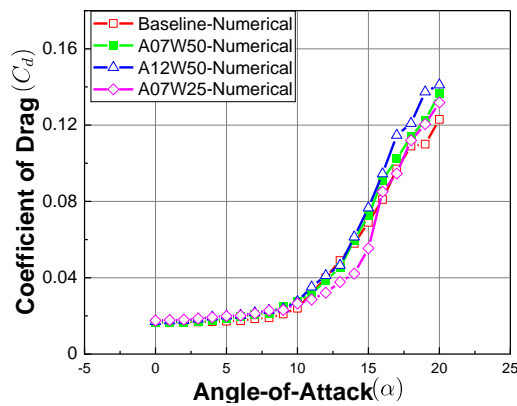
##### 4.1 Numerical Results: Aerodynamic Behavior

Figure 8a clearly represents the lift coefficient  $C_l$  with angles of attack  $\alpha$  for all four models simulated at  $Re=200000$ . All the models exhibited a finite non-zero lift coefficient at zero angles of attack thus depicting a relevant trend typical to any cambered airfoil. The zero lift coefficient  $C_{l,0}$  of baseline airfoil at  $Re=200000$  was recorded to be 0.2956 whereas A07W50, A12W50, and A07W25 began with marginally lower  $C_l$  values equaling to 0.2885, 0.2815, and 0.1995 respectively. With an increase in  $\alpha$ , all the models manifested quasi-linear  $C_l$  profiles up to  $8^\circ$ . Although the model A07W25 depicted a linearly rising trend,  $C_l$  was well below the baseline model for all the values up to  $8^\circ$ . In the linear region, the deviation in the slope  $dC_l/d\alpha$  was shallowly varying between  $0.13 \text{ deg}^{-1}$ - $0.08 \text{ deg}^{-1}$  for all the models. Above  $8^\circ$ , the  $C_l$  curve of the baseline model ceases to rise and displays a sluggishly rising behaviour. From this angle onwards, the lift coefficient of the baseline model deviates from linearity without any improvement in the lift coefficient. The stagnated  $C_l$  trend continues unyielding up to  $18^\circ$  beyond which the lift coefficient sharply declines indicating a complete stall. The numerical  $C_l$  values obtained in this study are seen to be coinciding supremely well with the experimental results for baseline S823 airfoil at  $Re=200000$  as reported in Selig *et al.* (1995). The

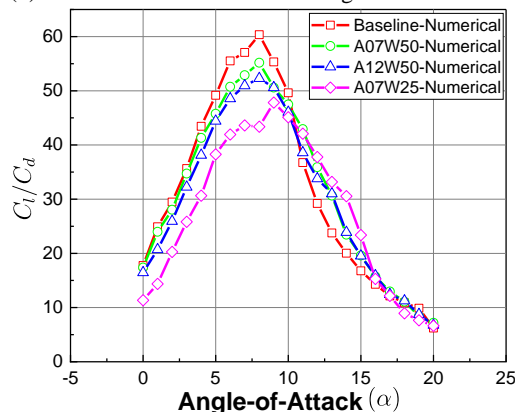
comparison clearly validates the numerical results for  $\alpha$  up to  $18^\circ$  but somewhat slightly deviates insignificantly at 19 and 20 degrees.



(a) Variation of Coefficient of Lift  $C_l$  with  $\alpha$ .



(b) Variation of Coefficient of Drag  $C_d$  with  $\alpha$



(c). Variation of  $C_l/C_d$  with  $\alpha$

**Fig. 8. Depiction of aerodynamic characteristics of S823 baseline and modified models at  $Re=200000$  achieved through numerical analysis.**

On the other hand, beyond  $8^\circ$ , surprisingly all the modified models displayed incremental  $C_l$  trend that was not observed for the baseline model. The slope of the  $C_l$  curves  $dC_l/d\alpha$  for the tubercled models continued to increase with shallow deviation from the constant state. This surge in  $C_l$  values for the modified models can be seen from 8- $15^\circ$  in Fig. 8a.

Maximum  $C_l$  recorded for the baseline model was 1.191 at  $10^\circ$ , but the  $C_l$  of the modified models surpassed the baseline model and was registered to be 1.4365, 1.5032, and 1.295 respectively which were 20.6%, 26.2% and 8.7% higher than the baseline model. Though the maximum  $C_l$  of A07W25 was lesser than A07W50 and A12W50, it was still found to be more than the baseline model. Alongside, even the maximum  $\alpha_{stall}$  for modified airfoils is seen to be pushed upwards  $15^\circ$  thus procrastinating the occurrence of flow separation and eventually enhancing the operational envelope of the airfoil. Post  $16^\circ$ , all the modified versions displayed a gradual downfall in the  $C_l$  trend implying the aggravation of flow separation phenomenon.

Variation of the drag coefficient  $C_d$  with  $\alpha$  for baseline and modified airfoils are provided in Fig. 8b. From the graph it is evidently seen that  $C_d$  for all the models are very coincidental throughout the scope of testing. A closer look at the graph reveals that beyond  $5^\circ$ ,  $C_d$  of the baseline model still remains essentially linear and slightly lower up to  $8^\circ$ , after which the drag coefficient starts to rise. However, the drag coefficient of modified models registered a deviation from linearity early at  $5^\circ$  later to which the drag is seen to increase. Among all, the lowest  $C_d$  is seen for the A07W25 model mostly between  $10^\circ$  and  $16^\circ$ . In the prestall and post stall region, A07W50 and A12W50 airfoils exhibit the highest  $C_d$ .

Next, the aerodynamic efficiency i.e., the lift-to-drag ratio for the models is portrayed in Fig. 8c. For the Reynolds number tested,  $C_l/C_d$  was comparatively highest for the baseline model. The baseline model expressed a maximum  $C_l/C_d=60.34$  at  $8^\circ$ . On the same lines A07W50, A12W50 and A07W25 models rendered maximum  $C_l/C_d=55.17$ ,  $C_l/C_d=52.259$ , and  $C_l/C_d=47.13$  independently at  $8^\circ$ . Post  $10^\circ$ , the baseline model started to manifest a downfall in the  $C_l/C_d$  ratio and the reduction is seen to be quite sudden. However, the same was not true for the modified models. The apparent effects of tubercles is quite noticeable on the modified models exclusively beyond  $10^\circ$  wherein all the models exhibited a moderate  $C_l/C_d$  and also continued to maintain it up to a wider operating range close to  $15^\circ$  after which it reduced gradually with restrained fall in  $C_l/C_d$  ratio. Similar to the  $C_l$  values, predictably, even the  $C_d$  and the  $C_l/C_d$  trends for the baseline model were in good agreement with the experimental results for the same Reynolds number as reported in Selig *et al.* (1995).

#### 4.4 Surface Velocity Distribution

Understanding how exactly the tubercles modify the flow over a tubercled model can be perceived visually from Fig. 9. The values obtained from the analysis are significantly a time-average quantity as the flow is considered to be turbulent. For clarity purpose, the surface velocity plot only at  $12^\circ$ ,  $14^\circ$  and  $16^\circ$  are highlighted for each modified model. It can be discerned from the images that the flow lines on the upper surface of the modified airfoils are no longer aligned axially with the streamwise flow

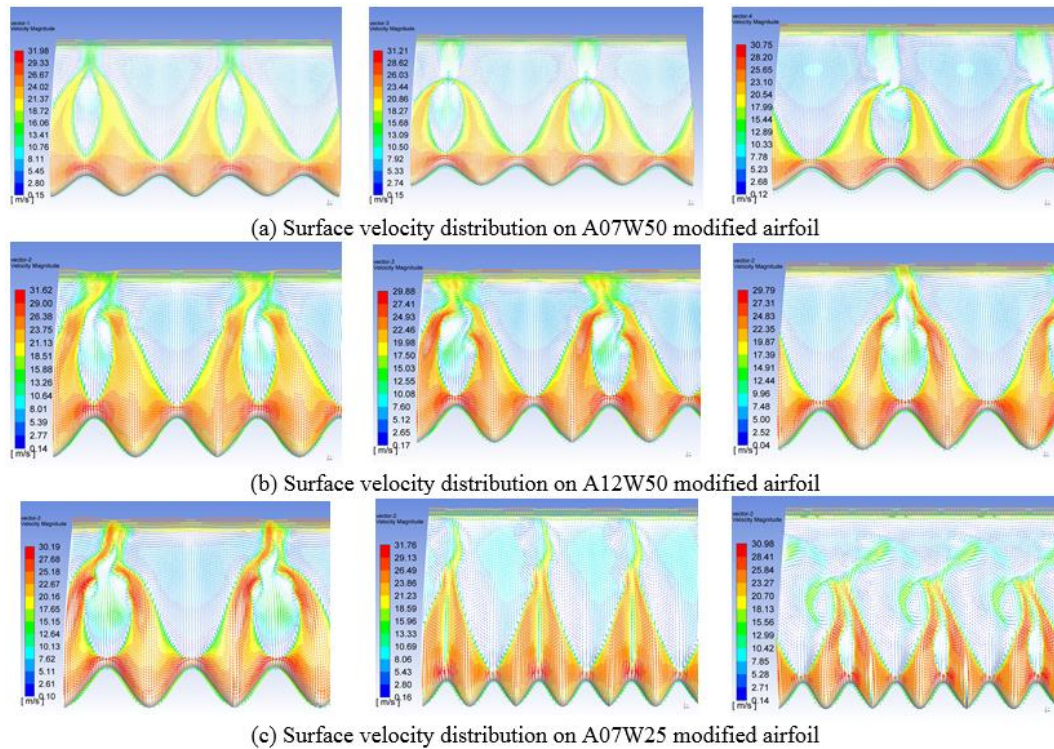


**Fig. 9. Surface Velocity Distribution on the Modified Models for  $Re=200000$  at  $12^\circ$ ,  $14^\circ$  &  $16^\circ$ .**

rather they tend to bend inwards at every pair of the tubercles. The inward bending fluid will ultimately merge together at every pair of tubercles and results in the formation of counter rotating vortices. The generation of streamwise vortices increases the mixing of fluid across the boundary layer and enhances the boundary layer momentum exchange, thus passively slowing flow separation process.

#### 4.5 Experimental Results

Based on the numerical assessment, the A07W50 model exhibited better aerodynamic characteristics over other modified airfoils. In view of this, the A07W50 model was finalized for further manufacturing and experimental testing. The model details have been provided in Fig. 7.

Figure 10a illustrates the  $C_l$  behavior of the baseline and A07W50 modified airfoils at  $Re=200000$  obtained experimentally. For the tested  $Re$ ,  $C_l$  of both the airfoils is visually coincidental up to  $3^\circ$ . At  $4^\circ$  the trend in the lift coefficient of the modified model deviates from the baseline model thus exhibiting higher lift values. The trend of the lift coefficient curve for the modified airfoil continued to grow linearly until  $\alpha$  reached  $9^\circ$ . Upwards  $9^\circ$  the lift coefficient of the modified model showed signs of slowing due to the emergence of flow separation phenomenon but however, it still continued to increase non-linearly until  $15^\circ$ . Extending the angles further, the modified models demonstrated a gradual reduction in the lift values, and the same is neatly indicated in the figure. On the flip side, the lift coefficient  $C_l$  demonstrated by the baseline model is noticeably lesser at every angle post 4

degrees. Maximum  $C_l=1.424$  was recorded at  $15^\circ$  for the modified model whereas the baseline model exhibited maximum  $C_l=1.1905$  at  $11^\circ$ .

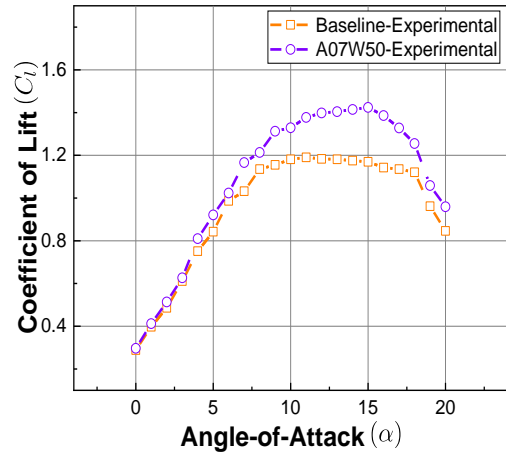
Figure 10b portrays the experimental behavior of drag coefficient  $C_d$  for the baseline and modified models at the  $Re=2e5$ . Graphically, it is evident that both the airfoils displayed closer drag values up to  $3^\circ$ . Hinging the angle upwards  $4^\circ$ , the drag coefficient of the modified airfoil is seen to increase slightly beyond the baseline model. Later the drag coefficient of both the airfoil continues to increase unabated suggesting the occurrence of flow separation.

The lift-to-drag ratio for the baseline and modified models estimated through wind tunnel testing is compared in Fig. 10c. It is clear from the figure that the maximum lift-to-drag for the baseline model is comparatively higher than the modified model. The maximum  $C_l/C_d=61.043$  for the baseline model is achieved at  $\alpha=8^\circ$ . But, the modified model demonstrated a maximum  $C_l/C_d=55.146$  at  $7^\circ$  angle of attack.

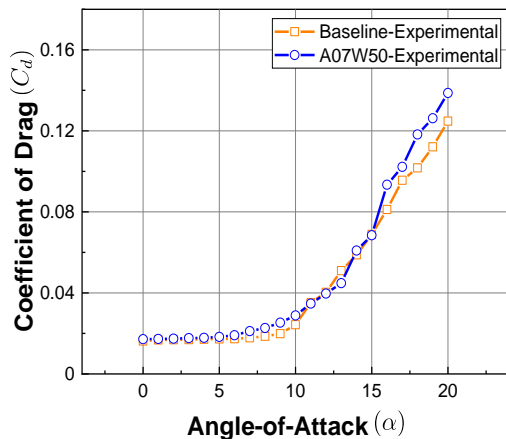
#### 4.6 Comparison of Experimental and Numerical Results

The aerodynamics characteristics of the baseline and A07W50 model at  $Re=200000$  tested numerically as well as experimentally are juxtaposed in Fig. 11. All the aerodynamic results obtained numerically are agreeing quite well with the experimental results and sequentially the experimental results obtained for the baseline model are also agreeing with the outcomes of S823 airfoil

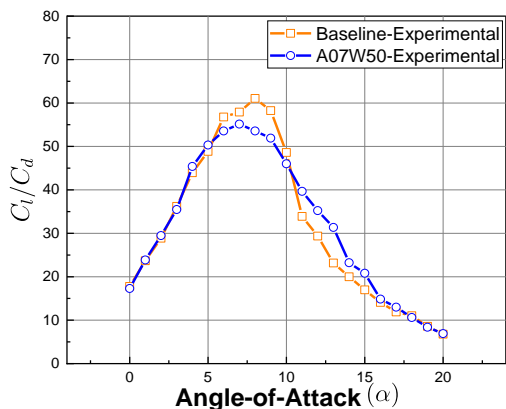
reported in Selig *et al.*(1995) for  $Re=200000$ . The consensus between the numerical and experimental outcomes evinced from the plots presented in Fig. 11 proves that the methodology implemented in the study is quite satisfactory.



(a) Experimental Lift Coefficient  $C_l$  with  $\alpha$  for baseline as well as modified models

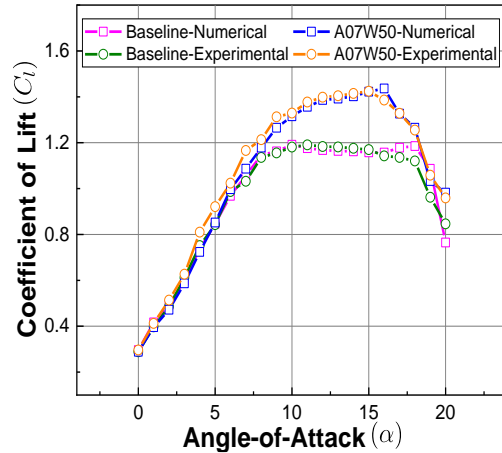


(b) Experimental Coefficient of drag  $C_d$  with  $\alpha$  for baseline and modified models

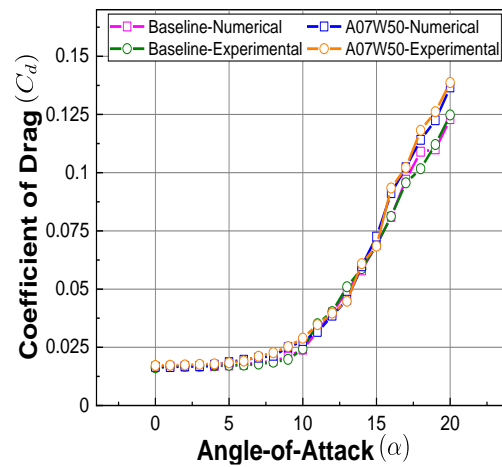


(c) Experimental results of  $C_l/C_d$  with  $\alpha$  for baseline and modified models

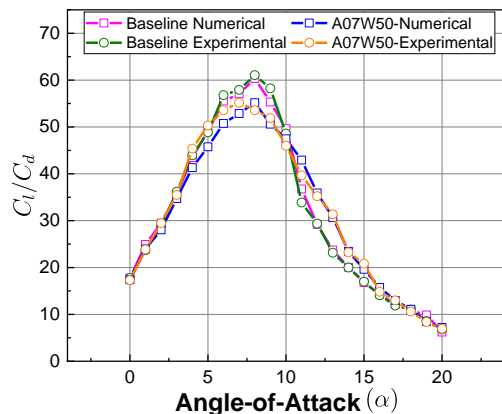
**Fig. 10. Representation of the aerodynamic behavior of S823 baseline and A07W50 modified models obtained experimentally.**



(a) Comparison of numerical and experimental Coefficient of Lift  $C_l$  with  $\alpha$



(b) Comparison of numerical and experimental Coefficient of drag  $C_d$  with  $\alpha$



(c) Comparison of numerical and experimental  $C_l/C_d$  with Angle-of-Attack  $\alpha$

**Fig. 11. Comparison of numerical and experimental aerodynamic results of baseline and A07W50 model performed at  $Re=200000$**

#### 4.7. Discussions of the Results

The performance trends of the baseline and modified airfoils viz., A07W50, A12W50 and A07W25 have been presented in the previous

sections. The effects of tubercles on the modified models definitely indicate favorable aerodynamic benefits, which can be perceived from the outcomes. The aerodynamic lift characteristics of all the models initially demonstrated a linearly increasing  $C_l$  behavior up to  $\alpha=5^\circ$  as shown in Fig. 8. Alongside, the slope of the lift curves also remained nearly the same for all the models. At shallow angles the adverse pressure gradients  $dp/dx > 0$  will be weak and near to the trailing edge and the fluid can easily surpass the negative pressures by consuming their kinetic energy. Here, the boundary layer will be thin and the flow will be attached to the suction side of the airfoil for angles up to  $5^\circ$  indicating a linearly increasing  $C_l$ . Furthering the attack angle increases the effective camber, leading to greater pressure differences that progressively increase the lift coefficients as seen for all the airfoils up to  $8^\circ$ . Extending the angles beyond  $8^\circ$  the lift coefficient for the baseline model completely drifts from linearity and subsequently slows down. The Sluggish lift coefficient surely indicates the tell-tale signs of the flow separation process that has just occurred on the airfoil.

At moderately large angles of attack as in our case occurring from  $8-18^\circ$  the adverse pressure gradients become progressively stronger wherein the fluid particles are required to move from a region of low pressure to high pressure against the natural fluidity. Fluids will naturally be accelerated only while moving from high pressure to low pressure regions (favourable pressure gradient) at the expense of pressure energy, but the reverse will occur while moving from low pressure to high pressure regions (adverse pressure gradient) wherein the fluid has to expend its kinetic energy to overcome strong pressures. Operating the airfoil at large angles, the pressures will be so enormous that the fluid particles in the boundary layer would no longer be capable of surpassing the pressure mountain and will naturally be brought to a complete rest as it would have expended all the kinetic energy. At this point, the fluid kinetic energy, as well as the tangential stresses applied by the particles, will reduce to zero i.e.,  $\tau = 0$ . The point on the airfoil surface, where the shear stresses becomes zero, is called flow separation point. Beyond this, the shear stresses become negative leading to flow reversal across the layers closer to the airfoil wall that in turn generate vortices and eddies in the wake region of the airfoil. All these problems will tend to thicken the boundary layer increasing the form drag projected by the airfoil that directly reduces the lift generation capacity of the airfoil thus making it more sluggish and stagnated without rising any further. Passive behaviour of the baseline model noticed from  $8-18^\circ$  in Fig. 8a conveys a pronounced effect in the flow separation process intertwined with apparent consequences of boundary layer thickening, progression of separation point and generation of form drag.

For angles beyond  $18^\circ$ , the pressure gradients

become unprecedentedly large. Unable to withstand strong pressure gradients, the flow separation point will quickly move towards the leading edge and completely separates leaving no flow attached to the suction side of the airfoil. In this situation, the generation of pressure differences will cease and the lift generation will rapidly decline to lead to a stall. The airfoil stalls in a manner similar to the leading edge stall. Stall is an extremely undesirable phenomenon to reckon with that leads to increase form drag coupled with the sudden loss of lift. Stall is generally characterized by the large separated flow. The boundary layer after separation will result in an additional flow phenomenon known as free shear layers that forms further downstream and leads to the formation of the wake with an unsteady flow in it. This unsteady character of the wake further increases the drag on the airfoil (Schlichting *et al.* 2017).

Opposingly, this nature of the  $C_l$  trend for the modified models is different from the baseline model that can clearly be differentiated from the figures. The  $C_l$  for all the tubercled models continued to increase from  $8-15^\circ$  without any significant reduction in the lift coefficient. Unyielding  $C_l$  with angle shows that all the tubercled models were superior in encountering the phenomenon of flow separation which was not seen on the baseline model. The  $C_l$  trend obtained for modified airfoils in this study is in positive agreement with the results demonstrated in Johari *et al.* (2007) which reported that the  $C_l$  for tubercled NACA634021 airfoil also manifested a gradual reduction in lift coefficient rather than traditional hard stall as represented in Miklosovic *et al.* (2014). The sole reason for the improved performance of the modified models is the presence of tubercles that were missing from the baseline model. If we isolate one single tubercle and analyze the flow over it, it can be surmised that the upfront geometrical protrusion of the tubercles effectively changes the leading edge sweep angle on either side of the tubercle at exactly  $\lambda/2$  i.e., at the peak of the tubercle. As a result, the flow which otherwise moves in the chord wise direction will no longer continue in that dimension rather it bends in the spanwise direction on either side of the tubercle as witnessed in fig 9. The spanwise bending flow will rotate in opposite directions resulting in the generation of localized vortices. Each tubercle always results in the generation of a pair of counter rotating vortices. The vortices stemming from the protuberances rotate in a way that causes them to migrate towards the valleys causing coalescence of fluid between protuberance peaks and tend to create low pressures in the valleys of the protuberances. This reduction in pressure in the valleys of the tubercles increases the overall pressure difference generated by the fluid flow. The spanwise flow between protuberances causes interactions between neighboring protuberances and generates a bi-periodic flow pattern along protuberances on the leading edge (Johari *et al.* 2007).

Further, the counter rotating localized vortices cause unstable asymmetric flow patterns making the flow to be very turbulent and chaotic. The high turbulent flow helps in enhancing the momentum exchange across the boundary layer and the flowing fluid and prevents the flow from separating (Johari *et al.* 2007) even at higher angles of attack despite encountering large adverse pressure gradients. The momentum carried is proportional to the strength of the vortices generated by the tubercles (Hugo *et al.* 2008). In doing so the tubercled models exhibit modest lift coefficients even at high angles of attack due to the prevention of flow separation from the suction side of the airfoil. The same can be inferred from 10b that the lift coefficients of all the modified models were extended beyond the capability of the baseline model. Additionally, the presence of tubercles also delayed the onset of stall, severity of stall and finally increased the overall operation envelope of the airfoil (Rostamzadeh *et al.* 2013). The counter rotating vortices springing from tubercles contain similar characteristics to the vortices that appear on a delta wing as reported in Goruney *et al.* 2009. Further, the tubercles are compared to vortex generators that enhance the boundary layer attachment through greater momentum exchanges Owen *et al.* (2001). However, Nierop *et al.* (2008) claim that since the wavelength and the amplitude of tubercles is always greater than the thickness of the boundary layer, they work differently than vortex generators.

From the study, it can be noted from Fig. 8a that the coefficient of lift is better for the tubercled model A12W50 which has the same wavelength but higher amplitude as compared to A07W50. Since both these models possess the same wavelength, from the current outcomes it can be implied that the amplitude of the tubercles might have a larger influence than wavelength on the aerodynamic characteristics of an airfoil and this agrees well with the outcomes of Johari *et al.* 2007. However Nierop *et al.* (2008) totally disagrees and stresses that the wavelength of a tubercle has a more pronounced effect on the performance of an airfoil or wing. For better clarity on this, additional experimentations are required that will eventually be taken up in the near future. At last, from the figure, the lift coefficient is seen to gradually diminish beyond 18° without any signs of an abrupt stall.

The drag coefficient projected in Fig. 8b shows that  $C_d$  for all the models are seen to hover around 0.015 at zero degree angle of attack where it is lowest. The finite non-zero coefficient of drag is due to the minimum surface area projected by the models at 0°. With angles incrementing, the coefficient of drag is seen to rise but remain almost coincidental up to 5 degree for all the models. This is because, at low angles, the separation point will be closer to the trailing edge with the resulting boundary layer being thin without any significant development of form drag. From 5-8°, the drag coefficient of

all the modified models in the graph is seen to slightly increase beyond the baseline model. The exiguous rise in drag coefficient  $C_d$  of all the modified airfoils can be attributed to the extra projected surfaces of the tubercles that increase the upfront area of the airfoil. After 8 degrees,  $C_d$  for the baseline model tends to rapidly increase and this surge in drag coefficient has an equivalent effect on the lift (passive behaviour of lift) of the baseline model that can be observed from 8-15° in Fig. 8a. When the baseline model operates between 8 and 15°, the thickness of the boundary layer grows significantly and leads to a tremendous rise in the form drag. Extending the angles further, the separation process speeds up and the drag begins to rise more rapidly until it reaches the stall angle. At  $\alpha_{stall}$  the drag increases precipitously with a sudden drop in the lift of the airfoil as observed from the graph. Comparatively, the drag coefficient  $C_d$  for the modified models is found to rise from 8° yet in a gradual manner. The enhanced boundary layer mixing caused by the tubercles prevents the flow from separating. The flow is found to be attached to the regions at the peak of the tubercles (Johari *et al.* 2007). In doing so, the tubercles retain the flow and the resulting boundary layer will be narrow, yielding a minimal form drag. This encompassing feature of the tubercles in minimizing the form drag will positively aid in improving the lift coefficients as observed across the angles 8-15° for the tubercled models in Fig. 8a. Later, escalating the attack angles, the drag coefficient for the modified models continued to rise gradually until the angle of attack reached 18° beyond which all the modified models stalled in a smooth manner.

Initial interpretation of the graphical outcomes from Fig. 8c reveals the performance of the baseline model to be better in comparison to the modified models. However, close observations will certainly convey performance differences in the graph where the baseline model is surely better within the prestall regime whereas the performance of the tubercled models is seen to dominate across the post stall regime. The baseline model exhibited a  $C_l/C_d$  equal to 60.34 at 8°, which is the largest among all the models across the entire test range. Comparatively A07W50, A12W50, and A07W25 models projected maximum  $C_l/C_d=55.17$ ,  $C_l/C_d=52.259$ , and  $C_l/C_d=47.13$  independently at 8°. The tubercled models viz., A07W50, A12W50 and A07W25 rendered a reduction in the aerodynamic efficiency of 8.56%, 13.39% and 21.89% respectively in the prestall range. Marching past  $\alpha=8^\circ$ , the aerodynamic efficiency of all the models gradually started to taper continuing up to 10°. However, the post stall regime (10°-20°) is indicative of the true performance of all the airfoils. Visual comparison of the  $C_l/C_d$  trends for all the models in Fig. 8c clearly signifies that the baseline model failed to generate any  $C_l/C_d$  in the post stall regime. This is because the boundary layer established on the baseline model would predominantly be laminar in nature. Laminar boundary layers can withstand only mild pressure

gradients at low and moderate angles of attack and are easily prone to separation. Consequently, they cannot generate any lift in the post stall regime which is accompanied by a large increase in form drag arisen due to the enlargement of the boundary layer comprised of vortices and eddies. The same can be noticed from the graph showing no improvement in the  $C_l/C_d$  values post  $8^\circ$ .

Conflictingly, though all the tubercled models depicted a falling  $C_l/C_d$  curve, it is good to highlight that the reduction presented by the tubercled models were very much gradual and restrained. The restrained fall in the  $C_l/C_d$  values post stall demonstrates the ability of the tubercled models in controlling the rate at which the lift values decrease with the accompaniment of slow increase in drag. Boundary layer energization caused by the tubercles makes the boundary layer to be highly turbulent. From boundary layer theory (Schlichting *et al.* 2017) we can understand that turbulent boundary layers are more tolerant towards large pressure gradients despite operating at moderately high angles of attack thus slowing down the flow separation process and aiding better aerodynamic characteristics to the lifting body. The same can be observed from Fig. 8c where all the modified models manifested greater  $C_l/C_d$  values up to 16 degrees angle. In the post stall regime between 10 and 16 degrees, the average aerodynamic efficiency of baseline as well as A07W50, A12W50 and A07W25 models were 27.20%, 30.83%, 29.82% and 32.47% respectively. This translated to an increase in the overall average aerodynamic efficiency of A07W50, A12W50, and A07W25 models by 13.30%, 9.63%, and 19.38% as compared to the baseline model. Finally, the enhancement in the  $C_l/C_d$  across the post stall regime positively widens the scope of operation of the tubercled models beyond the reach of the baseline model. This is a significant contribution rendered by biomimicking the humpback whale tubercle morphology on S823 airfoil for engineering applications.

## 5. CONCLUSIONS

Tubercles are surmised to be critical morphological features of the humpback whales that aid in adapting to the challenging environmental pressures. Despite their humungous size as well as weight, tubercles are believed to contribute to the maneuverability of the whale and help in hunting, lunging, feeding, etc thereby helping their survival in the toughest oceanic ecosystem. Through biomimicry, the concept of tubercles has been adapted in our study in an effort to ascertain the effect of tubercles on S823 engineered airfoil specifically designed for horizontal axis wind turbine blades.

The aerodynamic characteristics of the baseline and modified tubercled airfoils entirely composed of S823 cross sectional profile were numerically and experimentally investigated. Firstly, the models were numerically examined through  $k-\omega$  SST model in ANSYS FLUENT software at  $Re=200000$  and  $\alpha$

up to  $20^\circ$ . Later from the numerical results, the modified model exhibiting comparably superior aerodynamic behavior was fabricated and experimentally evaluated in a low speed wind tunnel. Based on the numerical and experimental outcomes, the following conclusions have been arrived at:

1. The lift coefficients  $C_l$  for the tubercled models were significantly higher in the prestall regime. Additionally, even in the post stall regime, the tubercled model rendered modest lift coefficients outperforming the baseline model which failed to register any improvement in lift values. The results show that tubercles help in improving the pre and post stall behaviour of the airfoil.
2. The drag coefficient  $C_d$  of the modified models was marginally more compared to the baseline model throughout the test. Nevertheless, the modified models exhibited a gradual increase in drag coefficient with associated restrained stall, thus, reducing the effect of abrupt increase in drag.
3. The aerodynamic efficiency of the baseline model was marginally better only across the prestall regime. However, beyond  $\alpha_{stall}$  the aerodynamic efficiency declined sharply with the manifestation of an irrevocable sudden hard stall. Contrarily, all the modified models rendered a slightly lesser  $C_l/C_d$  ratio in the prestall region. But post  $\alpha_{stall}$  the  $C_l/C_d$  ratio of all the modified models surpassed the baseline model. Alongside, they offered restrained as well as soft stalling characteristics to the airfoil which can totally be attributed to the presence of tubercles. This particular feature aids the airfoil with better tolerance towards drag reduction in the post stall regime, exhibiting sustained lift coefficients even at higher angles of attack, thus improving the operational envelope of the airfoil.

Altogether the experimental and numerical outcomes obtained in this study have concluded that the incorporation of tubercles on engineered airfoils impart better aerodynamic characteristics. The study also approves that S823 airfoil can be taken up for further aerodynamic evaluation associated with three-dimensional effects.

## ACKNOWLEDGEMENTS

The authors hereby express the indebtedness to Prof. Srinivasan S and Prof. Bhaskar K, Assistant Professors, Department of Aerospace Engineering, R V College of Engineering, Bengaluru, for being instrumental in bestowing cognitive significance, besides successful completion of this research article.

## REFERENCES

Akshoy R. P., S.Joshi, A. Jindal, S. P. Maurya and

- A. Jain (2013). *Experimental Studies of Active and Passive Flow Control Techniques Applied in a Twin Air-Intake*. Volume 2013, Article ID 523759, 8 pages.
- Bar-Cohen, Y. (ed.) (2006). *Biomimetics: biologically inspired technologies*. Boca Raton, FL: Taylor & Francis.
- Bharat, B. (2009). Biomimetics: lessons from nature – an overview. *Phil. Trans. R. Soc. A* 367, 1445–1486.
- Choi, H., H. Park, W. Sagong and S. Lee (2012). Biomimetic flow control based on morphological features of living creatures. *Physics of Fluids* 24, 121302.
- Ernst, A. van Nierop, S. Alben and M. P. Brenner. (2008). How Bumps on Whale Flippers Delay Stall: An Aerodynamic Model. *PRL* 100, 054502.
- Fish, F. E. (2006). Limits of nature and advances of technology in marine systems: what does biomimetics have to offer to aquatic robots? *Applied Bionics and Biomechanics* 3, 49–60.
- Fish, F. E. and G. Lauder (2013). *Not Just Going with the Flow*. American Scientist, Vol: 1012013 Sigma Xi, The Scientific Research Society. Reproduction
- Fish, F. E. and G. V. Lauder (2006). Lauder. Passive and Active Flow Control by Swimming Fishes and Mammals. *Annual Review of Fluid Mechanics* 38,193–224.
- Fish, F. E. and J. M. Battle (1995). Hydrodynamic design of the humpback whale flipper. *Journal of Morphology* 225, 51-60.
- Fish, F. E., L. E. Howle and M. M. Murry (2008). Hydrodynamic flow control in marine mammals. *Integrative and Comparative Biology* 48, 788–800.
- Fish, F. E., P. W. Weber, M. M. Murray and L. E. Howle (2011). Marine Applications of the Biomimetic Humpback Whale Flipper. *Marine Technology Society Journal* 45(4), 198-207.
- Gad-el-Hak, M. (1989). Flow Control. *Applied Mechanics Reviews* 42, 261-293.
- Gad-el-Hak, M. (1998). Modern Developments in Flow Control. *Applied Mechanics Reviews* 49, 365–379, 1996.
- Gad-el-Hak, M. and D. M. Bushnell (1991). Separation Control: Review. *Journal of Fluids Engineering* 113, 5-30.
- Goruney, T. and D. Rockwell (2009) Flow past a delta wing with a sinusoidal leading edge: near-surface topology and flow structure. *Experiments in Fluids* 47,321–331.
- Guerreiro, J. L. E. and J. M. M. Sousa (2012). Low-Reynolds-Number Effects in Passive Stall Control Using Sinusoidal Leading Edges. *AIAA Journal* 50(2).
- Hansen, K. L., R. M. Kelso and B. B. Dally (2009). The effect of leading edge tubercle Geometry on the performance of Different airfoils. *ExHFT-7*, 28 June – 03 July 2009, Krakow, Poland.
- Hugo, T., C. Pedro and M. H. Kobayashi. (2008). Numerical Study of stall delay on humpback whale flippers. *46th AIAA Aerospace Sciences Meeting and Exhibit*. Reno, Nevada.
- Jahanmiri, M. (2010). Active Flow Control: A Review. *Research report: 12*, ISSN 1652-8549.
- Johari, H., C. Henoeh, D. Custodio and A. Levshin (2007). Effects of leading edge protuberances on airfoil performance. *AIAA J* 45, 2634.
- Lohry, M. W., D. Clifton and L. Martinelli (2012). Characterization and Design of Tubercle Leading-Edge Wings. *Seventh International Conference on Computational Fluid Dynamics (ICCFD7)*, Big Island, Hawaii, July 9-13.
- Michael S. S., J. J. Guglielmo, A. P. Broeren and P. Giguere (1995). *Summary of Low-Speed Airfoil Data*, Volume 1 SoarTech Publications, Virginia Beach, Virginia.
- Miklosovic, D. S., M. M. Murray and L. E. Howle (2007). Experimental Evaluation of Sinusoidal Leading Edges. *Journal of Aircraft* 44(4), 1404–1408.
- Miklosovic, D. S., M. M. Murray, L. E. Howle and F. E. Fish (2014). Leading-edge tubercles delay stalls on humpback whale (Megaptera novaeangliae) flippers. *Physics of Fluids* 16, L39-L42.
- Moghaddam, T. and N. Banazadeh Neishabouri (2017). On the Active and Passive Flow Separation Control Techniques over Airfoils. *IOP Conf. Series: Materials Science and Engineering* 248. 012009
- Owen, J. C., P. W. Bearman and A. Szewczyk (2001). Passive Control of VIV with Drag Reduction. *Journal of Fluids and Structures* 15, 597-605.
- Rostamzadeh, N., R. M. Kelso, B. B. Dally and K. L. Hansen (2013). The effect of undulating leading-edge modifications on NACA 0021 airfoil characteristics. *Physics of Fluids* 25, 117101.
- Schlichting, H. (2017), Klaus Gersten. *Boundary-Layer Theory*, Ninth Edition, Springer-Verlag Berlin Heidelberg.
- Tangier, J. L. and D. M. Somers (1995). *NREL Airfoil Families for HAWTs*. NREL/TP-442-7109.
- Watts, P. and F. E. Fish (2001), The Influence of Passive, Leading Edge Tubercles on Wing Performance, *Proceedings of the Twelfth International Symposium on Unmanned Untethered Submersible Technology (UUST)*, UUST01, Autonomous Undersea Systems

R. Supreeth *et al.* / *JAFM*, Vol. 13, No. 6, pp. 1885-1899, 2020.

Inst., Lee, NH.

Weber, P. W., L. E. Howle, M. M. Murray and D. S. Miklosovic (2011). Computational evaluation of the performance of lifting surfaces with leading-edge protuberances. *Journal of Aircraft* 48(2).

Weichao, S., M. Atlar and R. Norman. (2017).

Detailed flow measurement of the field around tidal turbines with and without biomimetic leading-edge tubercles. *Renewable Energy* 111, 688e707.

Yu, Zanin, B., V. V. Kozlov and A. M. Pavlenko (2012). Control of flow separation from a model wing at low Reynolds numbers. *Fluid Dynamics* 47(3), 403–410.